Transition from three- to two-dimensional Ising superconductivity in few-layer $NbSe_2$ by proximity effect from van der Waals heterostacking

Prakiran Baidya,[1] Divya Sahani,[1] Hemanta Kumar Kundu,[2] Simrandeep Kaur,[1] Priya Tiwari,[1] Vivas Bagwe,[3] John Jesudasan,[3] Awadhesh Narayan,[4] Pratap Raychaudhuri,[3] and Aveek Bid[1]

[1]*Department of Physics, Indian Institute of Science, Bangalore 560012, India*

[2]*Weizmann Institute of Science, Rehovot 7610001, Israel*

[3]*Tata Institute of Fundamental Research, Mumbai 400005, India*

[4]*Solid State and Structural Chemistry unit, Indian Institute of Science, Bangalore 560012, India*

(Received 28 April 2021; revised 23 October 2021; accepted 26 October 2021; published 11 November 2021)

We report the experimental observation of Ising superconductivity in three-dimensional $NbSe_2$ stacked with single-layer MoS_2. The angular dependence of the upper critical magnetic field and the temperature dependence of the upper parallel critical field confirm the appearance of two-dimensional Ising superconductivity in three-dimensional $NbSe_2$ with a single-layer MoS_2 overlay. We show that the superconducting phase has strong Ising spin-orbit correlations which make the holes spin nondegenerate. Our observation of Ising superconductivity in heterostructures of few-layer $NbSe_2$ of thickness $\sim$15 nm with single-layer MoS_2 raises the interesting prospect of observing topological chiral superconductors with nontrivial Chern numbers in a momentum-space spin-split fermionic system.

DOI: 10.1103/PhysRevB.104.174510

I. INTRODUCTION

An important focus in condensed matter physics is on creating two-dimensional (2D) topological chiral superconductors (SCs) with nontrivial Chern numbers [1–4]. Naturally occurring topological SCs being rare [5,6], recent efforts have concentrated on inducing superconductivity in systems with strong spin-orbit coupling (SOC) [7]. The fundamental idea is that in a time-reversal-invariant noncentrosymmetric system with strong spin-valley locking, the spin degeneracy (in momentum space) of the fermions gets lifted. In such a system, when the chemical potential of the system lies in between the spin-split valence band maxima, repulsive interactions can lead to topological pairing mechanisms [8,9].

For a single atomic layer of a system with a hexagonal lattice, the measured in-plane critical magnetic field is significantly larger than the Pauli limit. The origin of this enhancement lies in the intrinsic Ising SOI (arising as a consequence of in-plane inversion symmetry breaking) in the layer. This SOC manifests itself as an effective out-of-plane Zeeman-like field, B_{SO} with opposite orientations at K and K' valleys. Thus, for a cooper pair in such a system, spin-valley locking leads to a large $B_{c2}^{||}$. Ising superconductivity is thus the most promising candidate for the observation of topological effects. This phenomena has earlier been observed in ionic-gated 2D MoS_2 [10,11] and in single-layer $NbSe_2$ [12].

Single-layer 2H-MoS_2 (hereafter referred to as SL-MoS_2), owing to its strong SOC [13], holds the promise of forming the base for such exotic SCs with tailor-made properties. There have been previous reports of Ising superconductivity induced in ionic-gated 2D-MoS_2 [10,11]. But both these methods suffer from certain inherent drawbacks—structural changes in the material, rapid degradation of the sample under ionic liquid, the difficulty of fabricating a complex device structure and a superconducting transition temperature much lower than theoretical predictions. Single-layer $NbSe_2$ degrades very rapidly on exposure to the ambient, making it unfeasible as the basis for complex device architectures. A practical path to overcome this hurdle is by engineering novel heterostructures of $NbSe_2$ with other materials having properties whose combination can give rise to an atmosphere stable Ising superconducting phase.

Additionally, in all cases, SL-MoS_2 had been electron doped to achieve the SC. Note that the strength of SOC (and the resulting spin-valley coupling and spin splitting of the bands) in single-layer transition metal dichalcogenides (TMDs) is significant in the valence band. This implies that to have spinless fermions, such a system must be hole doped [8,9]. A controllable mechanism of inducing 2D superconductivity in TMDs that can achieve relatively high transition temperatures while maintaining the long-term stability of the device is elusive.

In this paper, we report the observation of Ising superconductivity in few-layer $NbSe_2$($\sim$15 nm) with an overlayer of SL-MoS_2. Having both materials from the TMD family avoids many of the problems arising from lattice mismatch at the interface [14–17]. Through systematic magnetotransport measurements, we establish that the system develops an Ising superconductivity that is distinct from that of pristine $NbSe_2$. Though Ising superconductivity has been observed in ionic-gated MoS_2 [10,11] and in single-layer $NbSe_2$, our approach has distinct advantages over previous attempts in terms of yield, stability of the system, and is more amenable for the realization of complex device structures.

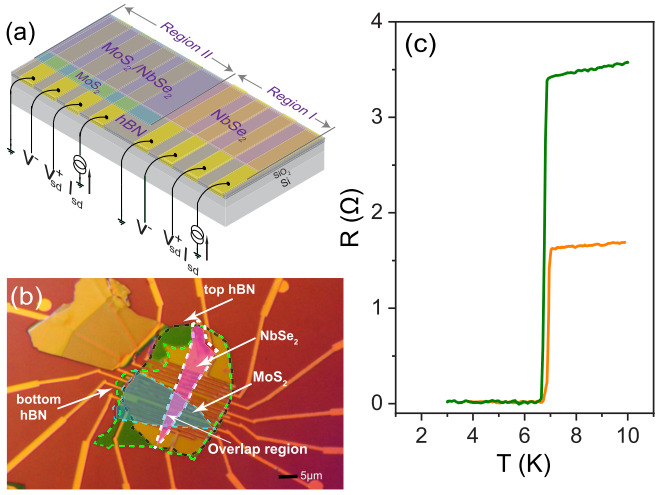

FIG. 1. (a) A schematic of the device structure. The SL-MoS_2 is transferred on top of gold contact pads etched in hBN. A multilayer $NbSe_2$ is transferred on top such that it lies partially on the MoS_2 (shown in light blue) and partially on the gold probes (shown as an orange rectangle). (b) False color differential interference contrast image of a final device. (c) Temperature dependence of the four-probe resistance of the pristine $NbSe_2$ (orange line) and of the SL-MoS_2 (olive line) sections of the device.

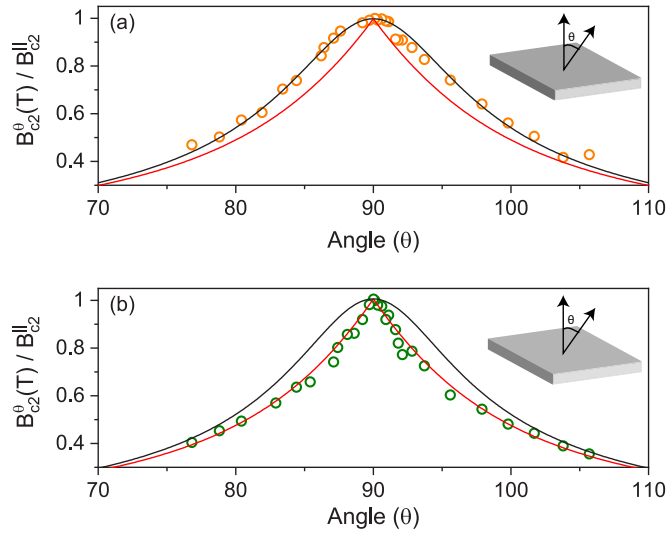

FIG. 2. Angular dependence of the B_{c2} for (a) region I and (b) region II. The red and black lines in both the panels are plots of 2D Tinkham model and 3D GL anisotropic mass model, respectively. The size of data points in both plots are larger than the error in the data. The insets show the direction of $B_{c2}(\theta)$.

II. DEVICE FABRICATION

The devices were fabricated by transfer of SL-MoS_2 using the dry transfer technique on gold probes prepatterned on a thick hBN substrate. This was followed by the transfer of a $NbSe_2$ flake (thickness ∼15 nm) such that it lay partially on the SL-MoS_2 and partially on the Au probes. We refer to the pristine $NbSe_2$ part of the device as region I and the SL-MoS_2/$NbSe_2$ heterostructure as region II. The entire device was capped with a thin flake of hBN (thickness ∼30 nm) to protect the device from environmental degradation (for details of device fabrication, see Appendix B). This device architecture allowed us to study electrical transport simultaneously in both the pure $NbSe_2$ and in the SL-MoS_2/ lying on top of $NbSe_2$ [Fig. 1(a)]. Figure 1(b) is the false-color optical image of a final device showing the SL-MoS_2 (blue area), the $NbSe_2$(∼ 15 nm) (pink area, region I), and the overlap area (region II).

III. RESULTS AND DISCUSSIONS

Electrical transport properties were measured in four-probe configurations using standard low-frequency lock-in detection techniques with an excitation current of 1μA in a dilution refrigerator. At room temperature and under zero gate bias, the SL-MoS_2 capped by $NbSe_2$ (region II) had significantly lower resistance (∼700 Ω) as compared to that measured for MoS_2 on SiO_2 or on hBN substrates (>1$M\Omega$) (data not shown). Figure 1(c) shows the temperature dependence of the resistance R of the two regions for $T < 10$ K—the resistances of both regions I and II decrease with decreasing temperature T before becoming smaller than our measurement resolution.

Figures 2(a) and 2(b) show the angle (measured with respect to the out-of-plane direction of the device) dependence of B_{c2} normalized by the in-plane B_{c2} at $T = 0.9T_c$ for regions II and I, respectively. The angular dependence of $B_{c2}(\theta)$ for region II is well described by the 2D Tinkham model $[(B_{c2}(\theta)|\cos\theta|/B^{\perp}_{c2}) + (B_{c2}(\theta)\sin\theta/B^{||}_{c2})^2 = 1]$ [18]. On the other hand, $B_{c2}(\theta)$ in the $NbSe_2$ region follows the 3D Ginzburg-Landau model $[(B_{c2}(\theta)\cos\theta/B^{\perp}_{c2})^2 + (B_{c2}(\theta)\sin\theta/B^{||}_{c2})^2 = 1]$ [19], establishing that in contrast to the 3D superconductivity of the pure $NbSe_2$ in region I, the superconductivity in region II is of 2D nature. This is the central point of this paper.

Having established that the SC in region II is 2D, we estimate the Berezinskii-Kosterlitz-Thouless transition temperature, T_{BKT} for region II from both nonlinear current-voltage characteristics and from the $R-T$ characteristics [20,21]) to be 6.14 K(see Appendix D for details).

Figures 3(a) and 3(b) show the normalized magnetoresistance as a function of a magnetic field applied in-plane for regions II and I, respectively. The in-plane critical field ($B^{||}_{c2}$) are plotted versus the reduced temperature, T/T_c in Fig. 3(c). Note that $B^{||}_{c2}$ for the region II is significantly larger than that of the pristine $NbSe_2$ in region I. The data from region II fits well with the 2D GL equation $B_{c2} = B_{c2}(0)\sqrt{1-T/T_c}$ [19], giving a $B^{||}_{c2}(0) \sim 36.5$ T. This is well beyond the Pauli paramagnetic limit, B_P (=∼1.86 T_c) ∼10.5 T for the system. For region I, the data, as expected for $NbSe_2$, flake thicker than the superconducting coherence length, fits with the 3D formula, $B_{c2} = B_{c2}(0)(1-T/T_c)$ [19]. The fact that the SC phase in region II has a dimension $d = 2$ (in contrast to $d = 3$ for $NbSe_2$ in region I) is the central result of this paper.

Figure 3(d) shows the plots of both $B^{||}_{c2}$ and $B^{\perp}_{c2}$ (normalized by B_P) versus the reduced temperature for region II. Here B_P (= 1.86 T_c) ∼ 10.5 T is the Pauli paramagnetic limit for the SL-MoS_2/$NbSe_2$ heterostructure. As can be seen, $B^{||}_{c2}(0)$ is ∼3.55 times above the Pauli limit. This is a direct indication of Ising superconductivity. The spin-splitting energy, $\Delta_{SO} \approx 2\,\mu_B B^{||}_{c2}(0)^2/B_P$ [12,22,23] estimated from the parallel-field

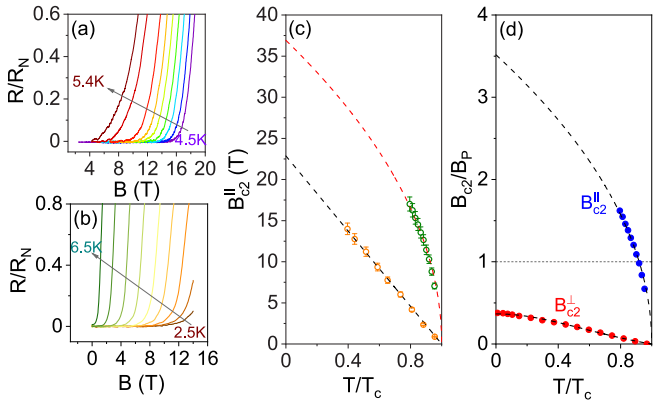

FIG. 3. Plot of magnetoresistance of (a) region I and (b) region II (normalized in both cases by the normal state resistance) for in-plane magnetic field. (c) Plot of $B_{c2}^{||}$ versus T/T_c for region I (green open circles) and region II (orange open circles) with the 2D GL fit (dashed red line) for region II and 3D fit (dashed black line) for region I. (d) Plot of B_{c2}/B_P versus T/T_c for both out-of-plane (red circle) and in-plane (blue circle) magnetic-field directions for region II—the dashed lines show the fits to the data.

magnetoresistance data was ∼15 meV which matches quite well with the theoretical estimation of Zeeman type SOI, $\Delta_{SO} \sim 13$ meV in 2D TMD [11].

To further distinguish between transport in the two regimes, we probed the vortex dynamics of the system through measurements of DC nonlinear current-voltage characteristics in the presence of an out-of-plane magnetic field, $B^{\perp}$. Figures 4(a) and 4(c) show the E-J characteristics for the two regions of the device measured at 2.5 K for different values of $B^{\perp}$ (the data for another device are presented in Fig. 11 of Appendix F). For a disordered SC in the flux-flow regime, the charge current density is given by $E = \rho_{ff}(J - J_p)$ [24], where E is the electric field between the voltage probes, ρ_{ff} is the flux flow resistivity, and J_p the depinning current density.

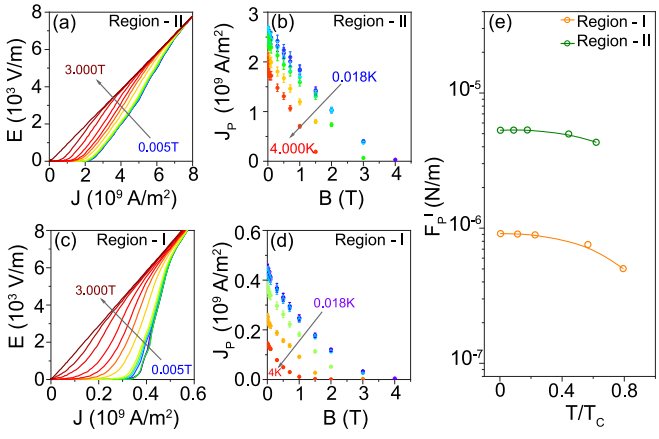

FIG. 4. $E - J$ characteristics at different $B^{\perp}$ measured at $T = 2.5$ K for (a) region II and (b) region I. Depinning current density J_p as a function of $B^{\perp}$ at 2.5 K for (c) region II and (d) region I. (e) Plots of the pinning force per unit length of the vortex, F_P^I versus the reduced temperature T/T_c region I (orange filled circles) and region II (olive filed circles). The lines are guides to the eye.

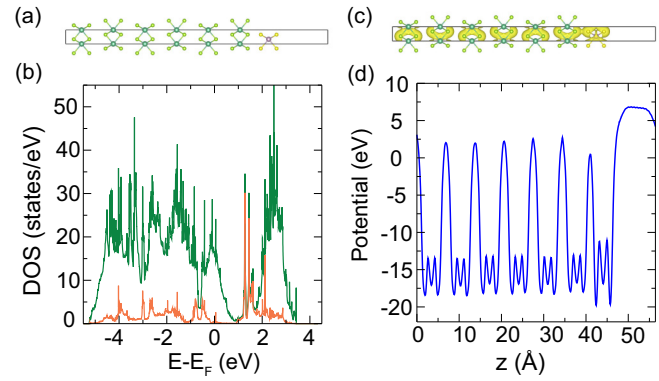

FIG. 5. (a) Illustration of the heterojunction with six layers of $NbSe_2$ and one layer of MoS_2. (b) The total density of states (olive) and density of states projected on the MoS_2 layer (orange) of the system. (c) Charge density isosurfaces for the heterojunction. (d) The average local potential along the stacking direction, z.

A comparison of Figs. 4(b) and 4(d) shows that J_P for the region II is much higher than that in region I. The pinning force per unit length of the vortex, extracted using the equation $F_P^I = J_p(h/2e)$ [25], is plotted in Fig. 4(e) at a few representative values of T/T_c. The value of F_P^I for region II is an order of magnitude higher than that of region I. This is expected given the significantly higher defect levels in SL-MoS_2 [26] as compared to that in $NbSe_2$. This establishes that in region II of the device, the presence of MoS_2 has a major effect on the transport of supercurrent through the underlying $NbSe_2$.

To recapitulate our principal results, we observe superconductivity at the heterojunction of SL-MoS_2 and few-layer $NbSe_2$(∼15 nm), which differs from that of $NbSe_2$ in several different aspects—the primary being its 2D Ising nature. We turn now to the discussion of the possible origin of this Ising SC.

A plausible mechanism is that the SL-MoS_2 can have cracks facilitating current to flow through it into the $NbSe_2$, This artifact was ruled out from atomic force microscopy (AFM) topography mappings on multiple devices, which did not show any structural damage on the SL-MoS_2 upon transfer on the prepatterned hBN probes (see Appendix C). An alternate proposition is that the transport in region II is solely through the underlying $NbSe_2$ whose superconducting properties change from that of 3D- to 2D-like due to the presence of the SL-MoS_2. We note that further experimental and theoretical studies are necessary to ascertain the mechanism of superconductivity in this hybrid system.

In an attempt to understand the effect of the presence of SL-MoS_2 on the superconductivity of the underlying $NbSe_2$, we carried out first-principles density functional theory calculations (see Appendix G for technical details). We constructed a heterojunction comprising of six layers of $NbSe_2$ and 1 layer of MoS_2, as shown in Fig. 5(a). The resulting density of states is presented in Fig. 5(b). The total density of states (olive curve) shows that the system is metallic, with many states around the Fermi level. We further calculate the density of states projected on the MoS_2 layer (orange curve). Notably, the MoS_2 layer also lost its semiconducting character when in proximity to the $NbSe_2$, as illustrated by the finite density of

states around the Fermi level on the MoS_2 layer. To further corroborate our findings, we present a plot of the charge density of the heterojunction in Fig. 5(c). The isosurfaces show substantial charge density at the various layers. Most notably, we find that the charge densities of the SL-MoS_2 layer and the $NbSe_2$ layer in contact with it are overlapping, confirming the hybridization between the two. This hybridization may result in the change in superconducting properties of $NbSe_2$ from 3D- to 2D-like, as we observed. From the Hall data in Appendix E, Fig. 10 the overlap of charge density is evident. We can also notice that the adding the SL-MoS_2 in region II varies the density from that of the pristine $NbSe_2$. The implication of this is that the coherence length of region II becomes larger than the typical ∼9 nm value of pristine $NbSe_2$, which consequently leads to the observation of 2D superconductivity in heterostructure.

An interesting observation is that the charge carriers in region II are holes—this is in accordance with previous observations [27]. Our observation that region II becomes a hole-doped 2D Ising SC is exciting because of the prospect that it can host a topologically nontrivial superconducting phase [8,9] and SCs with finite-momentum-pairing per the predictions by Fulde and Ferrell [28] and by Larkin and Ovchinnikov [29]. This makes our system unique; as in all earlier reports, a SC in TMD was achieved through electron doping [30].

IV. CONCLUSION

In summary, we have observed a transition from 3D to 2D superconductivity in heterostructures of few-layer $NbSe_2$ (∼15 nm) and SL-MoS_2. Magnetotransport measurements establish that the superconductivity in the underlying $NbSe_2$, albeit physically in the 3D limit, has a strong Ising pairing. The stability of the superconducting phase and the system being in the hole-doped region makes our device structure unique and opens up the scope of observing topological superconductivity in van der Waals systems.

ACKNOWLEDGMENTS

The authors acknowledge device fabrication facilities in National Nanofabrication centre, Centre for Nanoscience and Engineering, Indian Institute of Science. A.N. acknowledges support from startup Grant No. SG/MHRD-19-0001 of the Indian Institute of Science. A.B. acknowledges funding from SERB (No. HRR/2015/000017), DST (No. DST/SJF/PSA-01/2016-17), and IISc.

APPENDIX A: SUNKEN ELECTRICAL PROBES ON hBN SUBSTRATES

One disadvantage of dealing with TMD materials, especially $NbSe_2$, is their low stability in ambient conditions [31]. Keeping this fact in mind, we went for an encapsulated device structure (as described earlier). The flakes were transferred on prefabricated hBN sunken Au probes to avoid degradation due to exposure to moisture as chemicals such as e-beam resist, organic solvents, etc. The sunken probes also help avoid strain (usually present in such structures [32]) to the thin flakes of MoS_2 which may result in a tear that

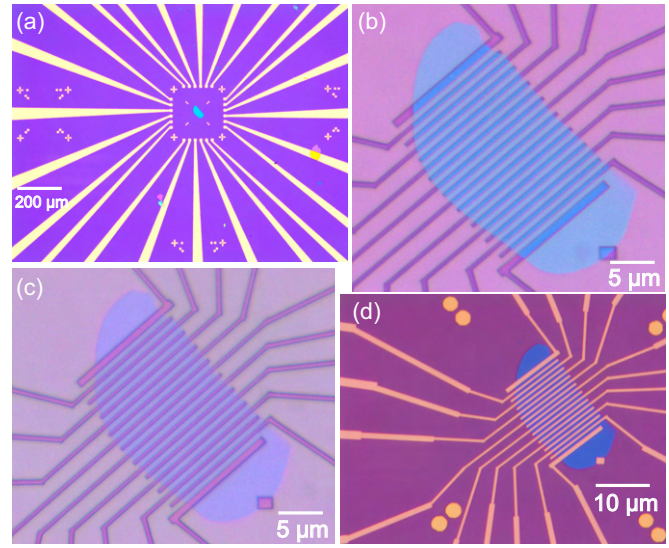

FIG. 6. Optical image at different stages of fabrication process of a hBN sunken Au probe (a) ∼25 nm hBN flake transferred on prepatterned substrate. (b) Electron-beam lithography patterns for contact on the hBN flake before dry etching. (c) The hBN flake after the dry etching process. (d) Final substrate after metal deposition.

can electrically short it with the $NbSe_2$ above it. So, for this purpose, we first fabricated a prepatterned substrate where big electrical contact pads of dimensions $\sim 200\,\mu m \times 200\,\mu m$ were initially patterned using photo-lithography technique on a ∼2 mm × 2 mm piece of a Si/SiO_2 substrate. The SiO_2 in the exposed region of the pattern were then etched by ∼45 nm using a Buffered HF solution with a subsequent step of deposition of Cr-Au of thickness 5-55 nm, respectively, creating big pads of an effective height of 15 nm with respect to the substrate surface. hBN flakes were procured using micromechanical exfoliation with a standard scotch-tape method [33] on commercial Polydimethylsiloxane (PDMS) gel stamp (Gel-Pak,PF-3-X4). Flakes of thickness ∼25 nm were roughly selected using optical microscope contrast. Selected flakes were then transferred using a micromanipulator and an optical microscope in the middle section of a prepatterned probe on a Si/SiO_2 substrate as shown in Fig. 6(a). After the transfer of hBN onto the substrate, the thickness of the flakes were confirmed using AFM technique and substrates having hBN flakes of thickness $\sim 25 \pm 2$ nm were only selected for further process. Subsequently patterns of electrical contacts on hBN as well as the connecting lines between hBN and the predeposited big pads were defined using e-beam lithography technique [Fig. 6(b)] with a follow-up step of selective etching of hBN using a proportionate mixture of CHF_3 and O_2 in a reactive ion etching system (RIE-Cl) to etch off the hBN in the exposed part of the flake along the contact lines as shown in Fig. 6(c). As the final step, Cr-Au of thickness 5–22 nm were then deposited giving an almost planar contact surface on hBN [Fig. 6(d)]. The advantage of having only 15 nm of effective height of big pads is that the connecting lines of total thickness of ∼27 nm would climb on top of it upon deposition ensuring continuous electrical connection. As a final step, the prepared probes were vacuum annealed at 250 °C for 3 h to get rid of any residue on the hBN surface before further process.

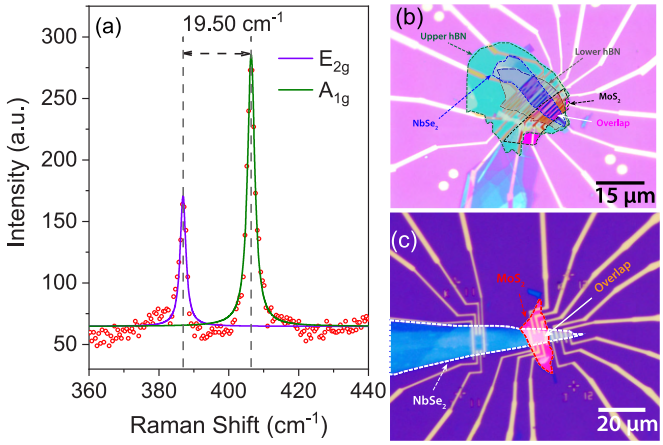

FIG. 7. (a) Room temperature Raman spectra of MoS_2 (red open circles) along with the Lorentzian fits for the E_{2g} peak (violet line) and A_{1g} peak (pink line). The difference in Raman Shift between the two peaks is 19.50 cm^{-1}, indicating the MoS_2 to be a single layer. False color optical image of few other measured devices in two different probe geometries. (b) Linear probe. (c) Hall measurement device for estimation of carrier no density discussed in Appendix E.

APPENDIX B: DETAILS OF DEVICE FABRICATION

Single-layer flakes of MoS_2 were obtained from high-quality single crystals by mechanical exfoliation [33] on PDMS gel stamp. The thickness of the flakes was verified through room-temperature Raman spectroscopy [34]. Figure 7(a) is the Raman spectra of one such MoS_2 flake, showing the presence of E_{2g} and A_{1g} peaks with a peak difference of $\sim$19.5 cm^{-1} in Raman shift confirming the flake to be a single layer [34]. The MoS_2 flake was transferred partially on the prepatterned Au contact probes on hBN (see Appendix A) using a dry transfer technique [35] with the help of a high-precision electrical micromanipulator and a digital camera fitted with an optical microscope. AFM measurements were carried out to rule out any cracks in the MoS_2 layer (see Appendix C).

$NbSe_2$ flakes were exfoliated in similar fashion in the inert environment of a glove box having O_2 and H_2O concentrations <0.5 ppm. The thickness of the flake was estimated to be $\sim$15 nm from optical contrast. The $NbSe_2$ flake was then transferred very precisely using the remote-controlled micromanipulator onto the probes such that half of the $NbSe_2$ flake lay on the exposed Au probes, whereas the other half got transferred on the SL-MoS_2. We refer to the region having only $NbSe_2$ as region I while the region with MoS_2 on $NbSe_2$ is referred to as region II. Finally, an hBN flake of thickness $\sim$30 nm was transferred to the device to avoid environmental degradation of the heterostructure. As a final step, the device was vacuum annealed at 200 °C to improve the coupling between the MoS_2 and $NbSe_2$ layers [36].

APPENDIX C: VERIFYING THE TOPOGRAPHY OF MoS_2 TRANSFERRED ON PROBES

To choose regions of defect-free SL-MoS_2, AFM measurements were carried out after transfer on the Au probes. Figure 8 shows an example of both the optical [Fig. 8(a)] and

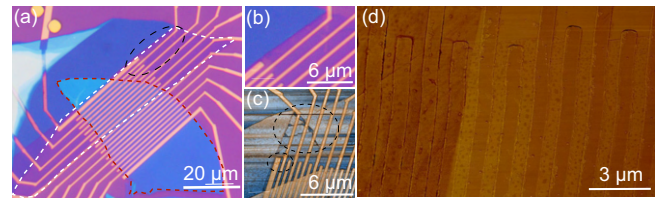

FIG. 8. (a) Optical image of monolayer of MoS_2 transferred on hBN sunken gold probes with false color dashed line showing the boundary of the MoS_2 (white) and hBN (red). The black dashed circle marks a region with cracks in the MoS_2 layer. (b) Zoomed-in image of the area marked by circle in Fig. 8(a) showing cracks in MoS_2 (c) AFM image of the system in enhanced coloring. (d) Zoomed-in AFM image of the section on probe showing MoS_2 on probe (darker shade) and bare probes (lighter shade).

AFM [Fig. 8(c)] images. The regions having cracks on MoS_2 (marked with blacked circles) as shown in Fig. 8(b) gives a contrast difference both in optical as well as AFM, which makes it easier to identify them. These areas were stringently avoided in making the final device. The zoomed-in image of SL-MoS_2 on the Au probes in Fig. 8(d) also shows the continuity of flakes. The few bubbles which are present in Fig. 8(d) were eliminated by the vacuum annealing after final assembly of the entire device.

APPENDIX D: ESTABLISHING BKT PHYSICS

In the main text, we have established, through angular dependence of the critical field, that in region II the superconductivity has an effective dimensionality of two. In this Appendix, we evaluate the Berezinskii-Kosterlitz-Thouless transition temperature, T_{BKT} of region II from the temperature-dependent current-voltage characteristics [Fig. 9(a)]. For a 2D SC, electric-field induced unbinding of the vortex-antivortex pairs give rise to nonlinear current-voltage characteristics of the form $V \sim I^{\alpha}$. At $T = T_{BKT}$, the nonlinearity exponent, α becomes 3 as shown in Fig. 9(b) [20,37]. This analysis yields $T_{BKT} = 6.13$ K.

One can also evaluate T_{BKT} from the R-T characteristics using the relation $R = R_0 \exp[-b_R/(T - T_{BKT})^{1/2}]$, where b_R is quantity indicating the vortex-antivortex interaction strength [20,21,38]. The formula is valid over a very small range of above T_{BKT} as within that range superconductivity is destroyed by thermal unbinding of vortex-antivortex pairs. Thus, by plotting its reduced form $(d \ln R/dT)^{-2/3} = (2/b_R)^{2/3}(T - T_{BKT})$, we can deduce the T_{BKT} from the x-axis intercept as shown in Fig. 9(c) which comes out to be 6.14 K. The estimation of T_{BKT} from both analyses is very close to the value of 6.3 K reported for ion-gated TMD in earlier results [10].

APPENDIX E: HALL MEASUREMENTS

Figures 10(a) and 10(b) show respectively the plots of R_{xy} versus B measured for regions I and II. The charge carrier densities calculated from these plots are shown Fig. 10(c). One can see that the estimated number densities in region II closely follows that of the pristine $NbSe_2$ in region-I.

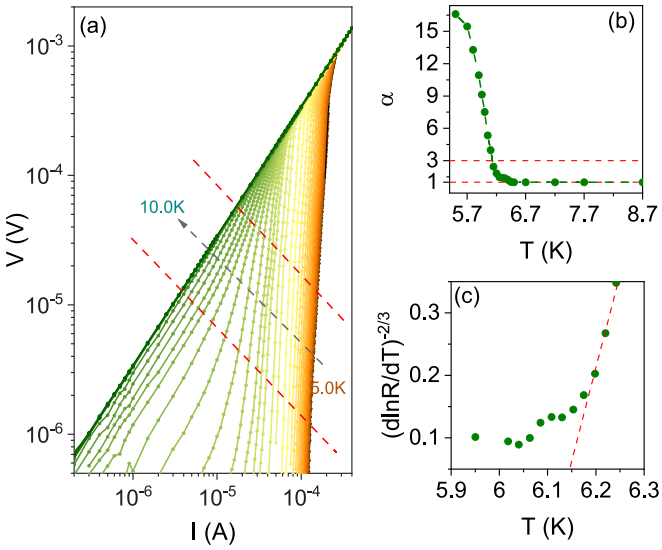

FIG. 9. (a) Zero magnetic field current-voltage characteristics of region II with varying temperature ranging from 5.0 K to 14.0 K. The red dashed line represents the range of current within which linear fit was done for each curve. (b) Plot of α as a function of temperature, T to evaluate T_{BKT} for region II. (c) Plot of $(d \ln R/dT)^{-2/3}$ as a function of temperature, T for the MoS_2 where the intersection of the black dashed line with the x axis gives T_{BKT}.

APPENDIX F: DEPINNING CURRENT, J_p EVALUATION

In Fig. 11 we present the data on another device. To obtain the depinning current, J_P we have to consider the linear section of the $E - J$ curve (Fig. 12) near the onset of resistance as following the definition, for $J > J_P$ the system enters into the flux flow regime for which the resistance, i.e., R_{ff} becomes independent of current [24]. For that purpose, we select a section of the curve just above the E value 1 V/m and perform a linear fit in that region. We then extract the value of J_P from the intersection of the best fit to the J axis [39], as shown in Fig. 12.

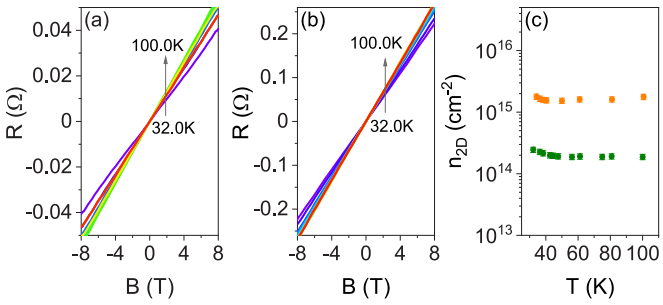

FIG. 10. Magnetic field (B) dependence of Hall resistance, R_{xy} for (a) region I over the temperature range 7.5 K–100 K and (b) region II over the temperature range 8 K–100 K. (c) Plot of the charge carrier density, n versus T for both region I (orange filled circles) and region II (olive filled circles) showing similar carrier densities, i.e., holes.

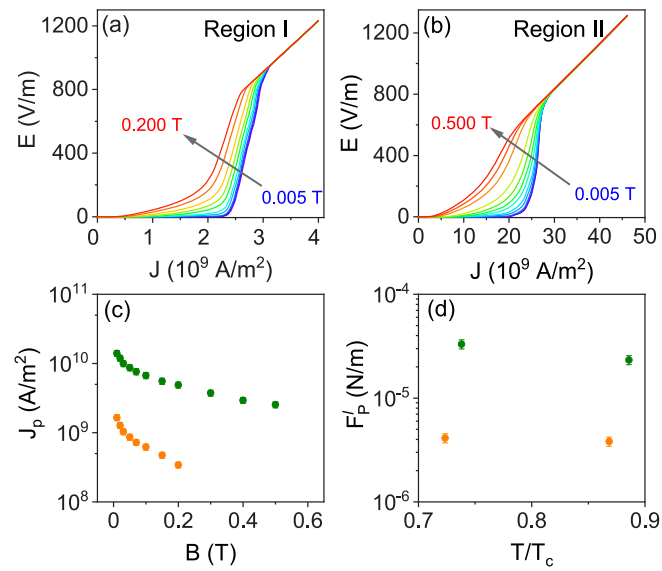

FIG. 11. $E - J$ characteristics at different perpendicular magnetic fields measured at $T = 5$ K for the (a) region I and (b) region II. (c) Depinning current density J_p as a function of the applied perpendicular magnetic field B at 5 K for region I (orange filled circles) and region I (green filed circles).(d) Plots of the pinning force per unit length of the vortex, F_P^l as a function of reduced temperature T/T_c for region I (orange filled circles) and region II (green filled circles).

APPENDIX G: *AB INITIO* CALCULATION

Density functional theory computations were performed using the VASP code [40,41]. The Perdew-Burke-Ernzerhof approximation to the exchange-correlation functional, including the van der Waals correction, was employed [42]. A plane-wave cutoff of 300 eV was used, and the Brillouin zone

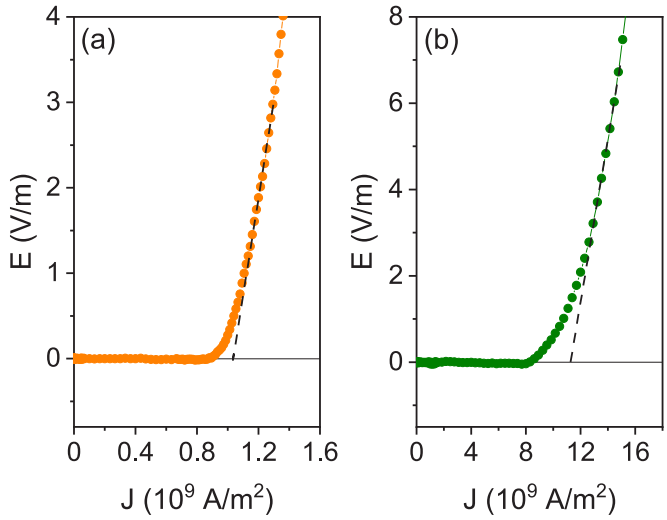

FIG. 12. $E - J$ characteristics at $T =$ 5 K and B=0.03 T for (a) region I and (b) region II. The dashed lines in both the plots are the linear fits—the intersection of this line with the J axis gives an estimate of the depinning current density.

was sampled using a $9 \times 9 \times 1$ Γ- centered k-point mesh. All atoms were relaxed until the forces were less than 0.01 eV/Å. A vacuum of 10 Å was used to avoid spurious interaction between periodic images.

[1] R. M. Lutchyn, E. P. Bakkers, L. P. Kouwenhoven, P. Krogstrup, C. M. Marcus, and Y. Oreg, Majorana zero modes in superconductor–semiconductor heterostructures, Nat. Rev. Mater. **3**, 52 (2018).

[2] S. M. Frolov, M. J. Manfra, and J. D. Sau, Topological superconductivity in hybrid devices, Nat. Phys. **16**, 718 (2020).

[3] C. Beenakker, Search for Majorana fermions in superconductors, Annu. Rev. Condens. Matter Phys. **4**, 113 (2013).

[4] S. Nadj-Perge, I. K. Drozdov, J. Li, H. Chen, S. Jeon, J. Seo, A. H. MacDonald, B. A. Bernevig, and A. Yazdani, Observation of Majorana fermions in ferromagnetic atomic chains on a superconductor, Science **346**, 602 (2014).

[5] C. Kallin, Chiral p-wave order in Sr_2RuO_4, Rep. Prog. Phys. **75**, 042501 (2012).

[6] C. Kallin and J. Berlinsky, Chiral superconductors, Rep. Prog. Phys. **79**, 054502 (2016).

[7] L. Fu and C. L. Kane, Superconducting Proximity Effect and Majorana Fermions at the Surface of a Topological Insulator, Phys. Rev. Lett. **100**, 096407 (2008).

[8] C. Triola, D. M. Badiane, A. V. Balatsky, and E. Rossi, General Conditions for Proximity-Induced Odd-Frequency Superconductivity in Two-Dimensional Electronic Systems, Phys. Rev. Lett. **116**, 257001 (2016).

[9] Y.-T. Hsu, A. Vaezi, M. H. Fischer, and E.-A. Kim, Topological superconductivity in monolayer transition metal dichalcogenides, Nat. Commun. **8**, 14985 (2017).

[10] J. Lu, O. Zheliuk, I. Leermakers, N. F. Yuan, U. Zeitler, K. T. Law, and J. Ye, Evidence for two-dimensional Ising superconductivity in gated MoS_2, Science **350**, 1353 (2015).

[11] Y. Saito, Y. Nakamura, M. S. Bahramy, Y. Kohama, J. Ye, Y. Kasahara, Y. Nakagawa, M. Onga, M. Tokunaga, T. Nojima *et al.*, Superconductivity protected by spin–valley locking in ion-gated MoS_2, Nat. Phys. **12**, 144 (2016).

[12] X. Xi, Z. Wang, W. Zhao, J.-H. Park, K. T. Law, H. Berger, L. Forró, J. Shan, and K. F. Mak, Ising pairing in superconducting $NbSe_2$ atomic layers, Nat. Phys. **12**, 139 (2016).

[13] Z. Y. Zhu, Y. C. Cheng, and U. Schwingenschlögl, Giant spin-orbit-induced spin splitting in two-dimensional transition-metal dichalcogenide semiconductors, Phys. Rev. B **84**, 153402 (2011).

[14] T. Yilmaz, I. Pletikosić, A. P. Weber, J. T. Sadowski, G. D. Gu, A. N. Caruso, B. Sinkovic, and T. Valla, Absence of a Proximity Effect for a Thin-Films of a Bi_2Se_3 Topological Insulator Grown on top of a $Bi_2Sr_2CaCu_2O_{8+\delta}$ Cuprate Superconductor, Phys. Rev. Lett. **113**, 067003 (2014).

[15] S.-Y. Xu, C. Liu, A. Richardella, I. Belopolski, N. Alidoust, M. Neupane, G. Bian, N. Samarth, and M. Z. Hasan, Fermi-level electronic structure of a topological-insulator/cuprate-superconductor based heterostructure in the superconducting proximity effect regime, Phys. Rev. B **90**, 085128 (2014).

[16] J. A. Hlevyack, S. Najafzadeh, M.-K. Lin, T. Hashimoto, T. Nagashima, A. Tsuzuki, A. Fukushima, C. Bareille, Y. Bai, P. Chen, R.-Y. Liu, Y. Li, D. Flötotto, J. Avila, J. N. Eckstein, S. Shin, K. Okazaki, and T.-C. Chiang, Massive Suppression of Proximity Pairing in Topological $(Bi_{1-x}Sb_x)_2Te_3$ Films on Niobium, Phys. Rev. Lett. **124**, 236402 (2020).

[17] D. J. Trainer, B. Wang, F. Bobba, N. Samuelson, X. Xi, J. Zasadzinski, J. Nieminen, A. Bansil, and M. Iavarone, Proximity-induced superconductivity in monolayer MoS_2, ACS Nano **14**, 2718 (2020).

[18] M. Tinkham, Effect of fluxoid quantization on transitions of superconducting films, Phys. Rev. **129**, 2413 (1963).

[19] M. Tinkham, *Introduction to Superconductivity* (Courier Corporation, Massachusetts, 2004).

[20] P. Minnhagen, The two-dimensional coulomb gas, vortex unbinding, and superfluid-superconducting films, Rev. Mod. Phys. **59**, 1001 (1987).

[21] D. Finotello and F. M. Gasparini, Universality of the Kosterlitz-Thouless Transition in He4 Films as a Function of Thickness, Phys. Rev. Lett. **55**, 2156 (1985).

[22] M. Sigrist, Introduction to unconventional superconductivity in non-centrosymmetric metals, in *Lectures on the Physics of Strongly Correlated Systems XIII: Thirteenth Training Course in the Physics of Strongly Correlated Systems*, AIP Conf. Proc. No. 1162 (American Institute of Physics, Maryland, 2009), pp. 55–96.

[23] S. J. Youn, M. H. Fischer, S. H. Rhim, M. Sigrist, and D. F. Agterberg, Role of strong spin-orbit coupling in the superconductivity of the hexagonal pnictide SrPtAs, Phys. Rev. B **85**, 220505(R) (2012).

[24] T. P. Orlando and K. A. Delin, *Foundation of Applied Superconductivity* (Addison-Wesley, Boston, Massachusetts, 1991).

[25] G. Blatter, M. V. Feigel'man, V. B. Geshkenbein, A. I. Larkin, and V. M. Vinokur, Vortices in high-temperature superconductors, Rev. Mod. Phys. **66**, 1125 (1994).

[26] S. Sarkar, A. Bid, K. L. Ganapathi, and S. Mohan, Probing defect states in few-layer MoS_2 by conductance fluctuation spectroscopy, Phys. Rev. B **99**, 245419 (2019).

[27] J. Guan, H.-J. Chuang, Z. Zhou, and D. Tománek, Optimizing charge injection across transition metal dichalcogenide heterojunctions: Theory and experiment, ACS Nano **11**, 3904 (2017).

[28] P. Fulde and R. A. Ferrell, Superconductivity in a strong spin-exchange field, Phys. Rev. **135**, A550 (1964).

[29] A. I. Larkin and Yu. N. Ovchinnikov, Nonuniform state of superconductors, Sov. Phys. JETP **20**, 762 (1965).

[30] J. Ye, Y. J. Zhang, R. Akashi, M. S. Bahramy, R. Arita, and Y. Iwasa, Superconducting dome in a gate-tuned band insulator, Science **338**, 1193 (2012).

[31] X. Xi, H. Berger, L. Forró, J. Shan, and K. F. Mak, Gate Tuning of Electronic Phase Transitions in Two-Dimensional $NbSe_2$, Phys. Rev. Lett. **117**, 106801 (2016).

[32] H. K. Kundu, S. Ray, K. Dolui, V. Bagwe, P. R. Choudhury, S. B. Krupanidhi, T. Das, P. Raychaudhuri, and A. Bid, Quantum Phase Transition in Few-Layer $NbSe_2$ Probed Through Quantized Conductance Fluctuations, Phys. Rev. Lett. **119**, 226802 (2017).

[33] K. S. Novoselov, A. K. Geim, S. V. Morozov, D. Jiang, Y. Zhang, S. V. Dubonos, I. V. Grigorieva, and A. A. Firsov, Electric field effect in atomically thin carbon films, Science **306**, 666 (2004).

[34] Q. H. Wang, K. Kalantar-Zadeh, A. Kis, J. N. Coleman, and M. S. Strano, Electronics and optoelectronics of two-dimensional transition metal dichalcogenides, Nat. Nanotechnol. **7**, 699 (2012).

[35] R. Yang, X. Zheng, Z. Wang, C. J. Miller, and P. X.-L. Feng, Multilayer MoS_2 transistors enabled by a facile dry-transfer technique and thermal annealing, J. Vac. Sci. Technol. **32**, 061203 (2014).

[36] S. Sarkar, H. Pradeepa, G. Nayak, L. Marty, J. Renard, J. Coraux, N. Bendiab, V. Bouchiat, J. K. Basu, and A. Bid, Evolution of inter-layer coupling in artificially stacked bilayer MoS_2, Nanoscale Adv. **1**, 4398 (2019).

[37] P. Minnhagen, Two-dimensional superconductors: Evidence of Coulomb-gas scaling, Phys. Rev. B **28**, 2463 (1983).

[38] V. Ambegaokar, B. I. Halperin, D. R. Nelson, and E. D. Siggia, Dynamics of superfluid films, Phys. Rev. B **21**, 1806 (1980).

[39] H. K. Kundu, K. R. Amin, J. Jesudasan, P. Raychaudhuri, S. Mukerjee, and A. Bid, Effect of dimensionality on the vortex dynamics in a type-II superconductor, Phys. Rev. B **100**, 174501 (2019).

[40] G. Kresse and J. Furthmüller, Efficiency of ab-initio total energy calculations for metals and semiconductors using a plane-wave basis set, Comput. Mater. Sci. **6**, 15 (1996).

[41] G. Kresse and J. Furthmüller, Efficient iterative schemes for ab initio total-energy calculations using a plane-wave basis set, Phys. Rev. B **54**, 11169 (1996).

[42] J. P. Perdew, K. Burke, and M. Ernzerhof, Generalized Gradient Approximation Made Simple, Phys. Rev. Lett. **77**, 3865 (1996).